

Contents lists available at ScienceDirect

Journal of the Mechanics and Physics of Solids

journal homepage: www.elsevier.com/locate/jmps





Dynamics of mechanical metamaterials: A framework to connect phonons, nonlinear periodic waves and solitons

Bolei Deng ^{a,1}, Jian Li ^{a,b,1}, Vincent Tournat ^c, Prashant K. Purohit ^{d,*}, Katia Bertoldi ^{a,*}

- ^a Harvard John A. Paulson School of Engineering and Applied Sciences, Harvard University, Cambridge, MA 02138, USA
- ^b Department of Engineering Mechanics, Zhejiang University, Hangzhou, 310027, China
- ^c Laboratoire d'Acoustique de l'Université du Mans (LAUM), UMR 6613, Institut d'Acoustique Graduate School (IA-GS), CNRS, Le Mans Université France
- d Department of Mechanical Engineering and Applied Mechanics, University of Pennsylvania Philadelphia, PA 19104, USA

ARTICLE INFO

Keywords: Flexible mechanical metamaterials Nonlinear dynamics Cnoidal waves

ABSTRACT

Flexible mechanical metamaterials have been recently shown to support a rich nonlinear dynamic response. In particular, it has been demonstrated that the behavior of rotating-square architected systems in the continuum limit can be described by nonlinear Klein–Gordon equations. Here, we report on a general class of solutions of these nonlinear Klein–Gordon equations, namely cnoidal waves based on the Jacobi elliptic functions sn, cn and dn. By analyzing theoretically and numerically their validity and stability in the design- and wave-parameter space, we show that these cnoidal wave solutions extend from linear waves (or phonons) to solitons, while covering also a wide family of nonlinear periodic waves. The presented results thus reunite under the same framework different concepts of linear and non-linear waves and offer a fertile ground for extending the range of possible control strategies for nonlinear elastic waves and vibrations.

1. Introduction

Mechanical metamaterials – engineered structures with mechanical properties governed by their geometry rather than composition – are attracting increasing interest as they facilitate behaviors not common in bulk, continuum media (Grima and Evans, 2000; Bertoldi et al., 2017; Christensen et al., 2015; Clausen et al., 2015; Lakes et al., 2001). Within the realm of dynamics, these systems are enabling control of mechanical waves in unprecedented ways (Bertoldi and Boyce, 2008; Wang et al., 2014). In the linearized regime periodic architectures engineered to support spectral gaps in frequency provide opportunities for the design of a wide range of functional devices, including wave guides and filters (Celli and Gonella, 2015), vibration insulators (Wang et al., 2016), energy harvesters (Chen et al., 2014a; Sun et al., 2010) and cloaks (Bückmann et al., 2015).

Although linear structures exhibit many interesting dynamic behaviors, the range of attainable wave propagation properties can be further expanded by considering nonlinear systems. As a first step in this direction, by applying a perturbation analysis, amplitude-dependent dispersion relationships have been predicted for architectures with weakly non-linear stiffness (Narisetti et al., 2010). Further, granular chains have been a convenient platform for highlighting amplitude-dependent phononic effects such as amplitude-dependent bandgaps or wave velocity (Cabaret et al., 2012, 2015), and dispersive second harmonic generation (Sánchez-Morcillo et al., 2013; Allein et al., 2020), among others (Melo et al., 2006; Theocharis et al., 2013). Finally, it has been recently

E-mail addresses: purohit@seas.penn.edu (P.K. Purohit), bertoldi@seas.harvard.edu (K. Bertoldi).

^{*} Corresponding authors.

These two authors contribute equally.

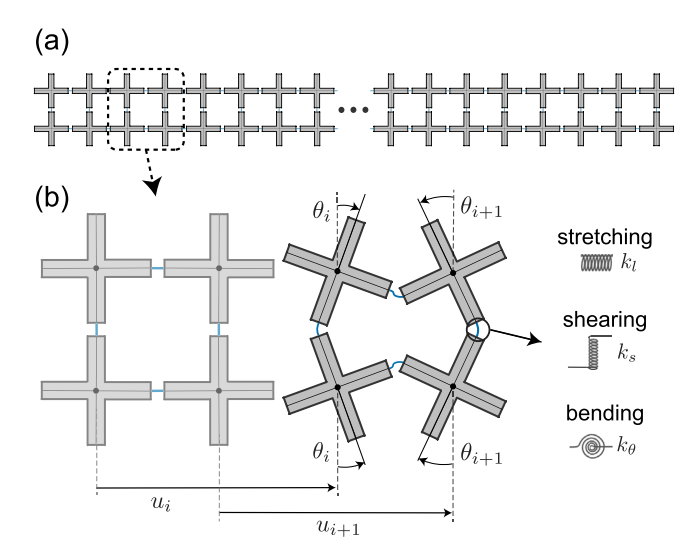


Fig. 1. (a) Schematics of the mechanical metamaterial considered in this study. (b) Discrete model based on rigid units connected at their vertices by springs.

demonstrated that flexible mechanical metamaterials can support the propagation of a variety of localized highly non-linear pulses, such as vector solitons (Deng et al., 2017, 2018b), topological solitons (Chen et al., 2014b; Deng et al., 2018a; Zhang et al., 2019) and rarefaction pulses (Yasuda et al., 2019; Deng et al., 2019c). However, while previous studies have almost exclusively focused either on periodic waves with small amplitude (i.e. linear and weakly non-linear waves) or non-linear pulses, the nonlinear dynamic behavior of flexible mechanical metamaterials is still largely unexplored and little is known about the propagation of large amplitude oscillatory traveling waves (Mo et al., 2019a).

Here, we present a framework based on cnoidal waves that provides a more complete and unified picture of the nonlinear dynamics of flexible mechanical metamaterials and enables us to systematically investigate the propagation and stability of phonons, solitons as well as large amplitude oscillatory traveling waves. To test our approach, we focus on a flexible metamaterial based on the rotating squares mechanism (Grima and Evans, 2000; Coulais et al., 2018; Deng et al., 2017), whose dynamic response in the continuum limit has been recently shown to be described by nonlinear Klein–Gordon equations (Deng et al., 2017, 2018b,a). While recent studies have focused on the solitary waves solution supported by this equation (Deng et al., 2017, 2018b,a), here we derive analytical solutions in terms of cnoidal waves – a general family of nonlinear solutions of Klein–Gordon equations – which reduce to phonons and solitons in two different limits. We first derive the continuum governing equations for the considered system, and focus on the effect of statically applied pre-compression. Then, we identify three forms of cnoidal wave solutions supported by the metamaterial and investigate the dependency of their characteristics on the applied precompression, both in the prebuckling and postbuckling regimes. Further, we numerically integrate the discrete and fully non-linear equations of motion to study each solution's stability, and ultimately obtain a phase diagram that identifies all stable solutions as a function of relevant wave and system parameters.

2. Governing equations

In this study we consider a long chain of N pairs of rigid crosses each with length a, mass m and rotational inertia J that are connected by thin and flexible hinges (see Fig. 1(a)). The chain is first subjected to a homogeneous static strain ε_{st} in the longitudinal direction (while preventing deformation in the transverse direction) and then elastic waves are initiated from its left end.

As recently shown in several studies (Deng et al., 2017, 2018b,a, 2019,b; Coulais et al., 2018), the response of such system can be accurately captured by modeling it as an array of rigid bodies connected via a combination of linear springs. Specifically, the ith pair of crosses is considered to be rigid and to have two degrees of freedom: the normalized displacement in the x-direction, U_i (the physical displacement is aU_i), and the rotation around the z-axis, θ_i (see Fig. 1(b)). As for the hinges, they are modeled by a combination of three linear springs: their longitudinal response is captured by an axial spring with stiffness k_i ; their shearing is captured by an axial spring with stiffness k_i ; their bending is captured by a torsional spring with stiffness k_θ (see Fig. 1(b)). When adopting such a discrete model, the dynamic response of the chain can be obtained by numerically integrating the 2N coupled differential equations obtained by writing the equations of motion for each top unit (see Appendix A — Eq. (49)). Further, the discrete equations of motion can serve as a basis to derive analytical solutions. To this end, we first take their continuum limit and assume that $\theta_i \ll 1$ to obtain

$$\frac{\partial^2 U}{\partial T^2} = \frac{\partial^2 U}{\partial X^2} + \theta \frac{\partial \theta}{\partial X},\tag{1a}$$

$$\frac{1}{\alpha^2} \frac{\partial^2 \theta}{\partial T^2} = \left(K_s - K_\theta \right) \frac{\partial^2 \theta}{\partial X^2} - 4 \left[\frac{3K_\theta}{2} + \frac{\partial U}{\partial X} \right] \theta - 2\theta^3, \tag{1b}$$

where X denotes the normalized position along the chain (the physical distance is X a), T is the normalized time (the physical time is $T\sqrt{m/k_I}$) and U(X,T) and $\theta(X,T)$ are two continuous functions interpolating the discrete variables such that $U(X=i,T)=U_i(T)$ and $\theta(X=i,T)=\theta_i(T)$. Moreover, $K_\theta=4k_\theta/(k_Ia^2)$, $K_s=k_s/k_I$ and $\alpha=a\sqrt{m/(4J)}$ are normalized parameters, which in this study we choose as $K_s=0.02$, $K_\theta=1.5\times10^{-4}$ and $\alpha=1.8$ (Deng et al., 2018b).

For the case of a quasi-static homogeneous deformation, the inertia terms can be neglected (i.e. $\partial^2/\partial T^2=0$) and both the rotation of the crosses and the longitudinal strain are spatially constant (i.e. $\theta=\theta_{st}$ and $\partial_X U=\varepsilon_{st}$, where θ_{st} and ε_{st} are the constant rotation and longitudinal strain). It follows that Eqs. (1) reduces to

$$\theta_{st}^3 + (3K_\theta + 2\varepsilon_{st})\theta_{st} = 0, \tag{2}$$

which we can numerically solve to obtain the relation between the applied strain ε_{st} and the resulting rotation of the crosses θ_{st} (note that, since Eq. (2) is derived from Eq. (1), such relation is valid only for $\theta_{st} \ll 1$). We find that Eq. (2) possesses two solutions with a bifurcation point at $\varepsilon_{st}^{cr} = -3/2K_{\theta} = -2.25 \times 10^{-4}$, so that

$$\theta_{st} = 0$$
, for $\varepsilon_{st} > \varepsilon_{st}^{cr}$,
$$\theta_{st} = \pm \sqrt{-2\left(\varepsilon_{st} + \frac{3}{2}K_{\theta}\right)}, \text{ for } \varepsilon_{st} < \varepsilon_{st}^{cr}.$$
(3)

Having analytically described the quasi-static response of the chain, we then seek solutions for the nonlinear waves supported by the predeformed system. Toward this end, we introduce the traveling wave coordinate $\zeta = X - cT$ (c being the normalized wave velocity) into Eq. (1) and integrate Eq. (1a) with respect to ζ to obtain

$$\frac{\partial U}{\partial \zeta} = -\frac{\theta^2}{2(1-c^2)} + C,\tag{4}$$

where C is an integration constant, which can be determined by imposing θ and $\partial U/\partial \zeta$ in the far field as $\zeta \to \infty$. Substitution of Eq. (4) into Eq. (1b) yields

$$\frac{d^2\theta}{d\zeta^2} = C_1\theta + C_3\theta^3,\tag{5}$$

where

$$C_1 = \frac{4\alpha^2}{c_0^2 - c^2} \left(C + \frac{3}{2} K_\theta \right), \text{ and } C_3 = -\frac{2\alpha^2 c^2}{(1 - c^2)(c_0^2 - c^2)},$$
 (6)

with $c_0 = \alpha \sqrt{K_s - K_\theta} \approx 0.254$. Note that C_1 and C_3 are coefficients with explicit expressions depending on the structural parameters and the applied pre-deformation. Physically, C_1 represents the effective linear dispersion coefficient and C_3 the coefficient of cubic non-linearity. Specifically, two different situations need to be considered.

• Case I: Prebuckling regime $(\varepsilon_{st} > \varepsilon_{st}^{cr})$

Prior to buckling,

$$\theta \to 0$$
 and $\partial U/\partial \zeta \to \varepsilon_{st}$ as $\zeta \to \infty$. (7)

It follows from Eq. (4) that

$$C = \epsilon_{st}$$
, (8)

and Eq. (6) specializes to

$$C_1 = \frac{4\alpha^2}{c_0^2 - c^2} \left(\epsilon_{st} + \frac{3}{2} K_\theta \right), \text{ and } C_3 = -\frac{2\alpha^2 c^2}{(1 - c^2)(c_0^2 - c^2)}.$$
 (9)

Note that in this regime (Fig. 2(a)),

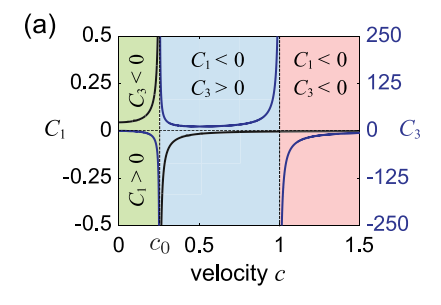
$$C_1 > 0$$
 and $C_3 < 0$ for $c \in (0, c_0)$,
 $C_1 < 0$ and $C_3 > 0$ for $c \in (c_0, 1)$,
 $C_1 < 0$ and $C_3 < 0$ for $c \in (1, \infty)$.

• Case II: Postbuckling regime ($\varepsilon_{st} < \varepsilon_{st}^{cr}$)
After buckling,

$$\theta \to \theta_{st}$$
 and $\partial U/\partial \zeta \to \varepsilon_{st}$ as $\zeta \to \infty$. (11)

It follows from Eq. (4) that

$$C = \frac{c^2 \theta_{st}^2}{2(1 - c^2)} - \frac{3}{2} K_{\theta},\tag{12}$$



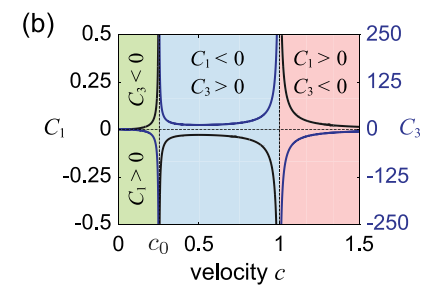


Fig. 2. C_1 and C_3 as a function of c for (a) the prebuckling regime (Eq. (9)) and (b) the postbuckling regime (Eq. (13)).

and Eq. (6) specializes to

$$C_1 = \frac{2\alpha^2 \theta_{st}^2 c^2}{(1 - c^2)(c_0^2 - c^2)}, \text{ and } C_3 = -\frac{2\alpha^2 c^2}{(1 - c^2)(c_0^2 - c^2)}.$$
 (13)

Note that in this regime (Fig. 2(b)),

$$C_1 > 0$$
 and $C_3 < 0$ for $c \in (0, c_0) \cup (1, \infty)$
 $C_1 < 0$ and $C_3 > 0$ for $c \in (c_0, 1)$. (14)

Eq. (5) has the form of the Klein–Gordon equation with third order non-linearity. While most recent studies have focused on its solitary wave solutions (Dauxois and Peyrard, 2006; Deng et al., 2017, 2018b,a), it has also been shown that it supports cnoidal wave solutions (Mo et al., 2019a). In the following we will investigate in details the cnoidal wave solutions supported by our system in both the prebuckling and postbuckling regimes.

3. Cnoidal wave solutions

The study of cnoidal waves has a long history dating back to the late 1800s when they were discovered as solutions to the Korteweg–de Vries equation (Whitham, 2011). Over the last century they have found applications in diverse fields from geophysical fluid dynamics (Clarke, 1971) to nonlinear optics (Wilson et al., 2011); the literature on this topic is vast and we do not attempt to review it here, but the interested reader may refer to some books (Samsonov, 2001; Remoissenet, 2013; Samsonov, 1994).

In this study we focus on Eq. (5) and find that it supports cnoidal wave solutions of the form

· dn solution:

$$\theta(\zeta) = A \, \mathrm{dn} \left(\frac{\zeta}{W} \middle| k \right), \tag{15}$$

where $dn(\cdot|k)$ is a type of elliptical function whose shape is controlled by the elliptic modulus k (0 < k^2 < 1, see Fig. 3(a)). Further, the wavelength of the dn wave solutions is related to k as

$$\lambda = 2K(k)W,\tag{16}$$

where K(k) is the complete elliptic integral of the first kind. Note that for $k \to 0$, Eq. (15) reduces to small amplitude vibrations (green line in Fig. 3(a)) and a single peak emerges in the frequency spectrum (green line in Fig. 3(b)). This linear monochromatic solution corresponds to the phonon limit. On the other hand, for $k \to 1$, Eq. (15) recovers the single soliton solution, $\theta(\zeta) = A \operatorname{sech}(\zeta/W)$ (red line in Fig. 3(a)), and has a broad continuous frequency content (red line in Fig. 3(b)). Finally, for intermediate values of k, Eq. (15) describes nonlinear periodic oscillations (blue line in Fig. 3(a)), so that the frequency spectrum shows higher order peaks at frequencies that are multiples of the fundamental one, i.e. harmonics (blue line in Fig. 3(b)). Furthermore, A and A0 are constants that can be determined by substituting the proposed solution into Eq. (5). Such dn wave solutions have physical amplitude defined as

$$\tilde{A} = \frac{1}{2} \left\{ \max \left[\theta(\zeta) \right] - \min \left[\theta(\zeta) \right] \right\} = \frac{1 - \sqrt{1 - k^2}}{2} A. \tag{17}$$

The translational component of the solution, $U(\zeta)$, is then found by substituting Eq. (15) into Eq. (4) and integrating it with respect to ζ ,

$$U(\zeta) = \int_{\zeta} \left(-\frac{\theta(\zeta')^2}{2(1 - c^2)} + C \right) d\zeta' = -\frac{A^2 W E \left(\phi \left(\frac{\zeta}{W} \middle| k \right) \right) \operatorname{dn} \left(\frac{\zeta}{W} \middle| k \right)}{2(1 - c^2) \sqrt{1 - k^2 \operatorname{sn} \left(\frac{\zeta}{W} \middle| k \right)^2}} + C\zeta + D, \tag{18}$$

where $\phi(\cdot|\cdot)$ is the Jacobi amplitude, $E(\cdot|\cdot)$ denotes the incomplete elliptic integral of the second kind and D is an integration constant (which corresponds to a rigid body motion). In practice, to generate cnoidal waves, a displacement given by Eq. (18) with the desired k can be imposed by a wave generator at one end of a sample, as described in Mo et al. (2019a).

· sn solution:

$$\theta(\zeta) = A \operatorname{sn}\left(\frac{\zeta}{W}\Big|k\right),\tag{19}$$

which reduces to harmonic vibrations, $\theta(\zeta) = A \sin(\zeta/W)$ for $k \to 0$ (green line in Figs. 3(c) and (d)), to a topological soliton $\theta(\zeta) = A \tanh(\zeta/W)$ for $k \to 1$ (red line in Figs. 3(c) and (d)), and to nonlinear periodic oscillations for intermediate values of k (blue line in Figs. 3(c) and (d)).

Note that the sn solution has physical amplitude

$$\tilde{A} = A,\tag{20}$$

wavelength

$$\lambda = 4K(k)W,\tag{21}$$

and that, by integrating Eq. (4), the translational component of the solution, $U(\zeta)$, is found as

$$U(\zeta) = \frac{A^2 W E\left(\phi\left(\frac{\zeta}{W}|k\right)\right) \sqrt{1 - k^2 \operatorname{sn}\left(\frac{\zeta}{W}|k\right)^2}}{2(1 - c^2)k^2 \operatorname{dn}\left(\frac{\zeta}{W}|k\right)} - \frac{A^2 \zeta}{2k^2(1 - c^2)} + C\zeta + D.$$
(22)

· cn solution:

$$\theta(\zeta) = A \operatorname{cn}\left(\frac{\zeta}{W} \middle| k\right),\tag{23}$$

which reduces to harmonic vibrations $\theta(\zeta) = A\cos(\zeta/W)$ for $k \to 0$ (green line in Figs. 3(e) and (f)), to a soliton $\theta(\zeta) = A \sec(\zeta/W)$ for $k \to 1$ (red line in Figs. 3(e) and (f)) and to nonlinear periodic oscillations for intermediate values of k (blue line in Figs. 3(e) and (f)).

Note that the cn solution has physical amplitude

$$\tilde{A} = A,$$
 (24)

wavelength

$$\lambda = 4K(k)W, \tag{25}$$

and that, by integrating Eq. (4), the translational component of the solution, $U(\zeta)$, is found as

$$U(\zeta) = -\frac{A^2 W E\left(\phi\left(\frac{\zeta}{W}|k\right)\right) \left[\frac{1-k^2}{k^2} + \text{cn}\left(\frac{\zeta}{W}|k\right)^2\right]}{2(1-c^2) \text{dn}\left(\frac{\zeta}{W}|k\right) \sqrt{1-k^2 \text{sn}\left(\frac{\zeta}{W}|k\right)^2}} + \frac{A^2(1-k^2)\zeta}{2k^2(1-c^2)} + C\zeta + D.$$
(26)

Importantly, as recently observed for solitary pulses (Deng et al., 2017, 2018b), Eqs. (15)–(18), (19)–(22) and (23)–(26) indicate that the system considered in this study supports the propagation of cnoidal waves with two components – one translational and one rotational – that are coupled together and copropagate. In the following, we focus on each solution separately, discuss in detail the relation between A, W, c and ε_{st} and investigate the stability of the identified wave solutions both in the prebuckling (i.e. $\varepsilon_{st} > \varepsilon_{st}^{cr}$) and postbuckling (i.e. $\varepsilon_{st} < \varepsilon_{st}^{cr}$) regimes. Finally, we want to point out that, although other types of cnoidal wave solutions exist (e.g., 1/dn, cn/dn and sn/dn), it can be shown that they all reduce to the cn, sn and dn solutions discussed here except for a phase shift (see Appendix C for details).

4. dn solution

We start by investigating the dn wave solution defined by Eq. (15). Substituting Eq. (15) into Eq. (5), we find that the latter is identically satisfied only if

$$2 = -A^2 W^2 C_1$$
 and $2 - k^2 = W^2 C_1$. (27)

Since the solutions given by Eq. (15) only exist if A and W are real, Eq. (27) indicates that our system can support the dn solution only if $C_1 > 0$.

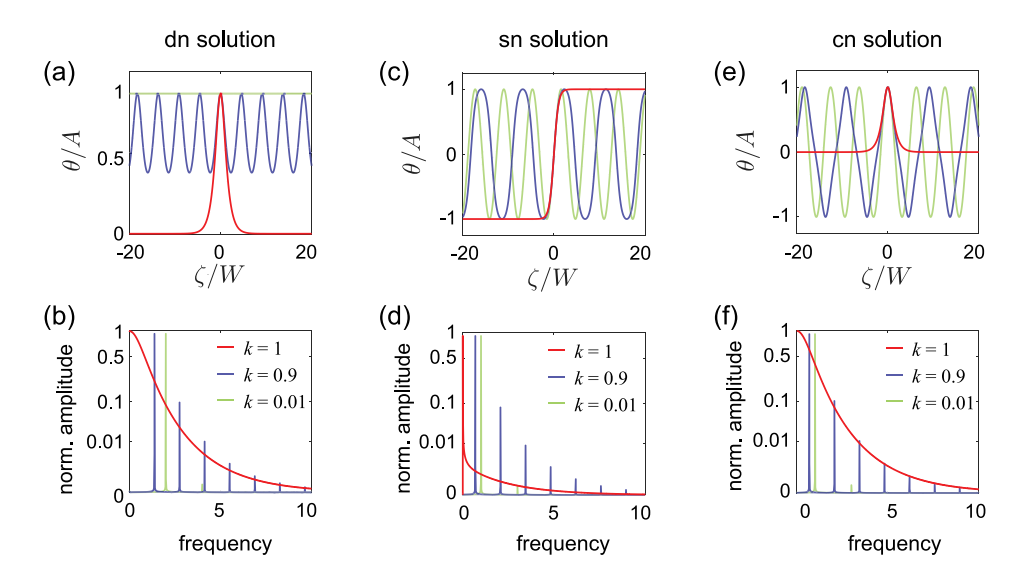


Fig. 3. (a)–(b) dn wave solution: (a) solution and (b) frequency spectrum for k = 1, 0.9 and 0.01. (c)–(d) sn wave solution: (c) solution and (d) frequency spectrum for k = 1, 0.9 and 0.01. (For interpretation of the references to color in this figure legend, the reader is referred to the web version of this article.)

4.1. Prebuckling regime

Eq. (10) indicates that prior to buckling $C_1 > 0$ for $c \in (0, c_0)$. As such, in this regime the dn solution exists only for $c \in (0, c_0)$ (see yellow and green areas in Fig. 4(a)). By substituting Eq. (9) into Eqs. (27) we obtain

$$A = \frac{2}{c} \sqrt{\frac{1 - c^2}{2 - k^2} \left(\epsilon_{st} + \frac{3}{2} K_{\theta}\right)} \text{ and } W = \sqrt{\frac{(c_0^2 - c^2)(2 - k^2)}{4\alpha^2 \left(\epsilon_{st} + \frac{3}{2} K_{\theta}\right)}}.$$
 (28)

In Fig. 4(b) we show the evolution of both physical amplitude \tilde{A} (defined by Eq. (17)) and W as a function of the wave speed c and the elliptic modulus k predicted by Eqs. (28) for $\varepsilon_{st} = 0$. We find that W is mostly affected by c and monotonically decreases as the wave speed becomes larger. As for \tilde{A} , it is found to become very large for $k \to 1$ and $c \to 0$. However, it is important to recognize that not all solutions described by Eqs. (15) and (28) are stable. To investigate the stability of the derived dn solutions, we numerically integrate the discrete equations of motion for the chain when applying the theoretical solution to the first unit (see Appendix A for details). More specifically, in our numerical analysis we consider a chain comprising N = 2000 units (to minimize boundary effects) and impose the following boundary conditions at the first unit (while leaving the other end free)

$$\theta_1(T) = \theta(\zeta = 1 - c(T - T_0)),$$

$$U_1(T) = U(\zeta = 1 - c(T - T_0)) + \varepsilon_{st} c(T - T_0).$$
(29)

where θ and U are the analytical solutions presented in Eqs. (15)–(26) and T_0 is a time shift introduced to make sure the boundary conditions are compatible with the initial ones. To characterize the stability of the dn solutions, we then compare the rotational components predicted by the analytical and numerical solutions for the first two hundred units as

$$err(T) = \frac{1}{200} \sum_{i=1}^{200} d \left[\Theta_i(T), \Theta(X, T) \right], \tag{30}$$

where $d[\mathbf{x}, A]$ represents the distance between a point with coordinates \mathbf{x} and the closest point on the curve A (D'Errico, 2013). Further,

$$\Theta_i(T) = \left[\frac{i}{200}, \tilde{\theta}_i(T)\right] \text{ and } \Theta(X, T) = \left[\frac{X}{200}, \tilde{\theta}(X, T)\right],$$
(31)

where $\tilde{\theta}_i(T)$ and $\tilde{\theta}(X,T)$ are the numerical and analytical solutions normalized to vary between -0.5 and 0.5. We consider a solution to be stable if err(T) < 0.001 in any time window [T,T+100] for the entire duration of the simulation. Using this criterion, we find that in the prebuckling regime the dn solution leads to stable waves only for $k \to 1$ (see the green area in Fig. 4(a) and region bounded by the green lines in Fig. 4(b)).

To further validate the predictions of our continuum model, in Fig. 4(c) we compare analytically (lines) and numerically (markers) predicted rotations profiles at $\varepsilon_{st} = 0$ for different combinations of c and k. In general, for the solutions that are predicted to be stable we observe an excellent agreement between the discrete and continuum models. For k = 1 both analytical and numerical

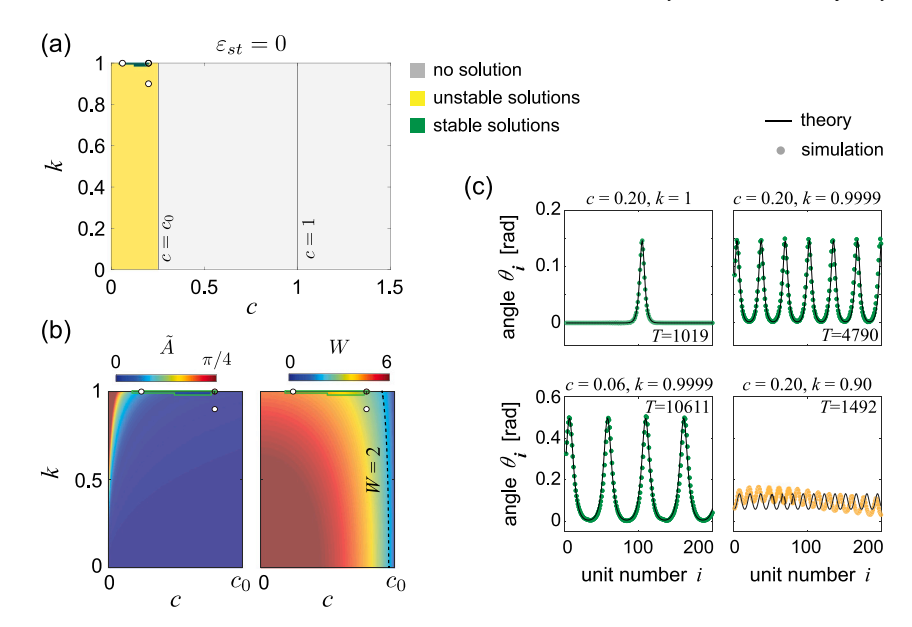


Fig. 4. (a) Effect of c and k on the dn wave solutions supported by the metamaterial in the prebuckling regime. (b) Evolution of \tilde{A} and W as a function of c and k at $\epsilon_{st} = 0$. (c) Numerical (markers) and analytical (lines) results for dn solutions propagating in an undeformed chain (i.e. $\epsilon_{st} = 0$). Rotation profiles for (c, k) = (0.20, 1), (0.20, 0.9999), (0.06, 0.9999) and (0.2, 0.9). The circular markers in Figs. 4(a) and (b) indicate the points considered in our numerical analysis, whose results are presented in Fig. 4(c). (For interpretation of the references to color in this figure legend, the reader is referred to the web version of this article.)

results perfectly match and predict the propagation of a soliton (see the plot for c=0.20 and k=1 in Fig. 4(c). As k is slightly reduced to 0.9999, trains of solitons emerge which are captured by both the analytical and numerical solutions (see plots for k=0.9999 and c=0.20 and 0.06 in Fig. 4(c)). However, these solitary waves become unstable as $c\to 0$ and $c\to c_0$, since for these limits the physical amplitude \tilde{A} becomes too large (so that assumption $\theta\ll 1$ is violated) and width W too small compared to the unit cell size, so that the continuum limit is violated (note that the continuum approximation breaks when W<2 (Deng et al., 2018a) — see Fig. 4(b) where the contour line W=2 is highlighted). Finally, as k is further decreased the peaks become closer to each other forming oscillatory waves that are not stable (see plots for k=0.9 and k=0.20 in Fig. 4(c)). Such behavior may be attributed to a modulational instability of the nonlinear system, typical of the nonlinear Schrodinger equation (Parkes, 1991; Dauxois and Peyrard, 2006). Although this instability could also be theoretically investigated, such analysis would require a large body of work, which is beyond the scope of this paper.

4.2. Postbuckling regime

Eq. (14) indicates that in the postbuckling regime $C_1 > 0$ for $c \in (0, c_0)$ and $c \in (1, \infty)$, so that dn solution exists only for these ranges of c (see yellow and green areas in Fig. 5(a)). Note that the breakdown of the continuum solution as $c \to c_0$ and $c \to 1$ is due to imaginary width. By substituting Eq. (13) into Eqs. (27) we find that in these two regions

$$A = \sqrt{\frac{2}{2 - k^2}} \theta_{st} \text{ and } W = \sqrt{\frac{(c_0^2 - c^2)(1 - c^2)(2 - k^2)}{2\alpha^2 \theta_{st}^2 c^2}}.$$
 (32)

In Figs. 5(b) and (c) we report the evolution of both \tilde{A} (defined by Eq. (17)) and W as a function of c and k at $\varepsilon_{st}=-1.5\times 10^{-3}$ for both velocity intervals in which the solution exists. Note that since $\varepsilon_{st}=-1.5\times 10^{-3}<\varepsilon_{st}^{cr}$, Eq. (3) predicts all crosses to be pre-rotated by an angle $\theta_{st}=\pm 0.05$ before the waves start to propagate. The plots indicate that in both intervals \tilde{A} is not affected by c and monotonically increases with k. On the other hand, W is mostly affected by the wave speed and monotonically decreases with it for $c \in (0, c_0)$ and increases for $c \in (1, \infty)$. Further, by using Eq. (30), we find that for $\varepsilon_{st}=-1.5\times 10^{-3}$ almost all dn solutions with $c \in (0, c_0)$ are stable (see the green area in Fig. 5(a) and plots in Fig. 5(d) for (c, k) = (0.2, 1), (0.2, 0.71) and (0.2, 0.1)). However, a small region of unstable solutions exists for $k \to 1$ and $c \to c_0$. These unstable solutions correspond to solitary pulses with very small width, which violate the continuum assumption (see the plot for (c, k) = (0.24, 0.98) in Fig. 5(d). Differently, for $c \in (1, \infty)$ only solutions with $k \to 0$ are stable and these are characterized by small amplitude (see Fig. 5(c)). As a next step, we then investigate whether such small amplitude cnoidal solutions correspond well to the linear waves limit. Toward this end, the wave frequency in the limit of $k \to 0$ can be obtained as

$$\lim_{k \to 0} \omega = \lim_{k \to 0} \frac{2\pi c}{\lambda} = \frac{2\alpha c^2 \theta_{st}}{\sqrt{\left[\alpha^2 \left(K_s - K_\theta\right) - c^2\right] \left(1 - c^2\right)}}.$$
(33)

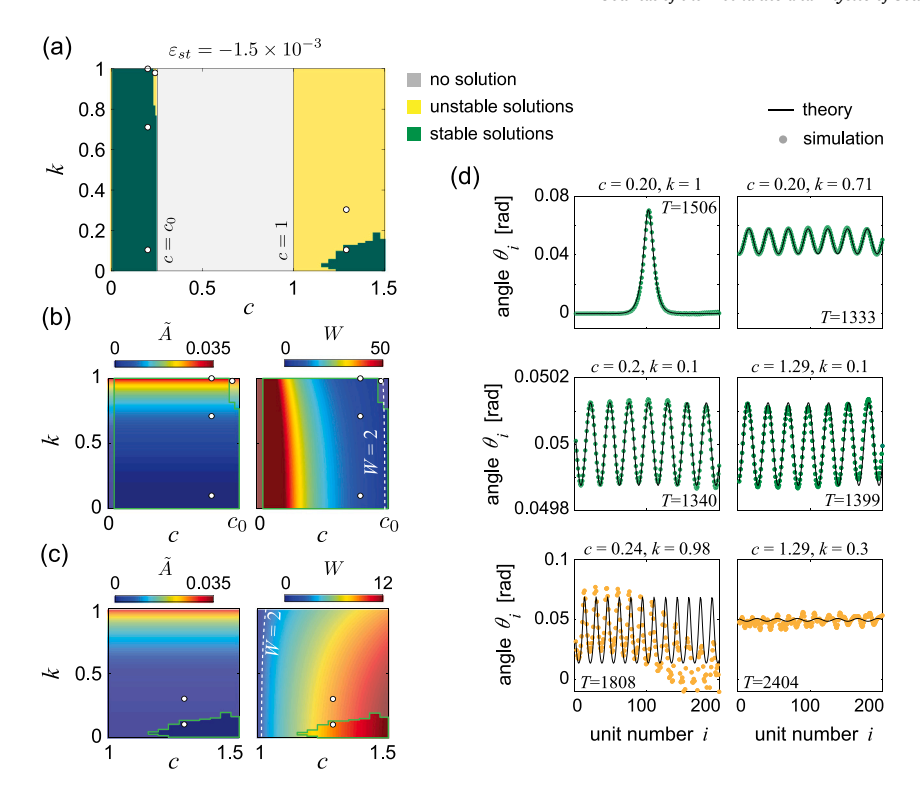


Fig. 5. (a) Effect of c and k on the dn wave solutions supported by the metamaterial in the postbuckling regime. (b)–(c) Evolution of \tilde{A} and W as a function of c and k at $\epsilon_{st} = -1.5 \times 10^{-3}$ (with $\theta_{st} = \pm 0.05$).(d) Numerical (markers) and analytical (lines) results for dn solutions propagating in a buckled chain (i.e. $\epsilon_{st} = -1.5 \times 10^{-3}$). Rotation profiles for (c, k) = (0.20, 1), (0.20, 0.71), (0.20, 0.10), (1.29, 0.10), (0.24, 0.98) and (1.29, 0.3). The circular markers in Figs. 5(a)–(c) indicate the points considered in our numerical analysis, whose results are presented in Fig. 5(d). (For interpretation of the references to color in this figure legend, the reader is referred to the web version of this article.)

where λ is the wavelength defined in Eq. (16). By expressing the wave speed as $c = \omega/\mu$ (where μ is the wave number), Eq. (33) can be rewritten as

$$\omega^4 - \left[\mu^2 + \alpha^2 (K_s - K_\theta)\mu^2 + 4\alpha^2 \theta_{\rm rl}^2\right] \omega^2 + \alpha^2 (K_s - K_\theta)\mu^4 = 0,\tag{34}$$

from which we obtain

$$\omega^{(1)} = \frac{\sqrt{2}}{2} \sqrt{D_1 - D_2} \text{ or } \omega^{(2)} = \frac{\sqrt{2}}{2} \sqrt{D_1 + D_2},$$
(35)

where

$$D_{1} = \mu^{2} + \alpha^{2} (K_{s} - K_{\theta}) \mu^{2} + 4\alpha^{2} \theta_{st}^{2},$$

$$D_{2} = \sqrt{D_{1}^{2} - 4\alpha^{2} (K_{s} - K_{\theta}) \mu^{4}}.$$
(36)

Eqs. (35) are the dispersion relations of the dn wave solution in the limit $k \to 0$. In Fig. 6 we compare these dispersion relations (dashed lines) to the ones derived directly from the linearized discrete equations of motion (solid lines — see Appendix B for the derivations). We find very good agreement between the two in the long wavelength regime (for shorter wavelengths the continuum assumption used to derive our analytical solution is not valid anymore). As such, these results indicate that the small amplitude waves to which the dn solution reduces to for $k \to 0$ are linear dispersive waves. Note that, since the rotational and translational components are coupled for linear waves in the postbuckling regime (see Appendix B), the cnoidal wave solutions are able to recover both branches at different velocity ranges.

5. sn solution

By substituting the expression of sn solution Eq. (19) into Eq. (5), we have

$$2k^2 = A^2W^2C_3$$
 and $1 + k^2 = -W^2C_1$. (37)

As such, Eq. (5) can support the sn solution only if $C_1 < 0$ and $C_3 > 0$.

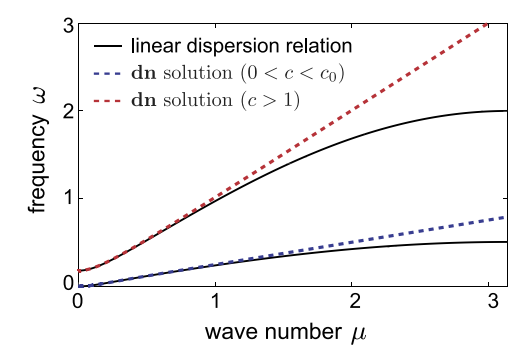


Fig. 6. Dispersion relation derived from cnoidal wave solutions (dashed lines) and the linearized discrete governing equations (solid lines) for a buckled chain with $\epsilon_{st} = -1.5 \times 10^{-3}$ (i.e. $\theta_{st} = \pm 0.05$).

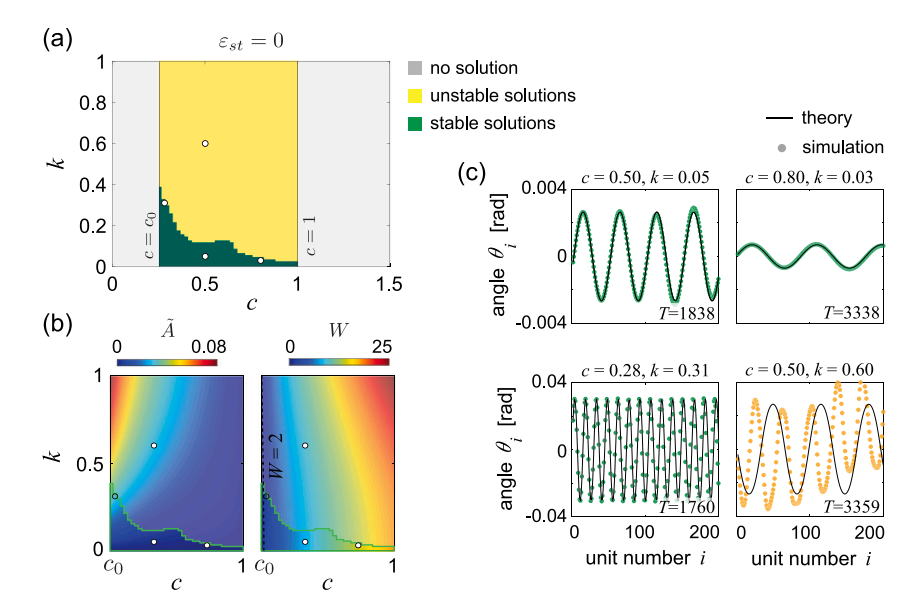


Fig. 7. (a) Effect of c and k on the sn wave solutions supported by the metamaterial in the prebuckling regime. (b) Evolution of \tilde{A} and W as a function of c and k at $\epsilon_{st}=0$. (c) Numerical (markers) and analytical (lines) results for sn solutions propagating in an undeformed chain (i.e. $\epsilon_{st}=0$). Rotation profiles for (c, k)=(0.50, 0.05), (0.80, 0.03), (0.28, 0.31) and (0.50, 0.60). The circular markers in Figs. 7(a) and (b) indicate the points considered in our numerical analysis, whose results are presented in Fig. 7(c). (For interpretation of the references to color in this figure legend, the reader is referred to the web version of this article.)

5.1. Prebuckling regime

According to Eq. (10), prior to buckling, such a solution exists in the velocity range $c \in (c_0, 1)$ (see yellow and green areas in Fig. 7(a)). Note that the breakdown of the continuum solution as $c \to c_0$ and $c \to 1$ is due to imaginary width and imaginary physical amplitude, respectively. By substituting Eqs. (9) into Eqs. (37), A, W for this deformation regime are obtained as

$$A = \frac{2k}{c} \sqrt{\frac{1 - c^2}{1 + k^2} \left(\varepsilon_{st} + \frac{3}{2} K_{\theta}\right)} \text{ and } W = \sqrt{\frac{(c^2 - c_0^2)(1 + k^2)}{4\alpha^2 \left(\varepsilon_{st} + \frac{3}{2} K_{\theta}\right)}}.$$
 (38)

In Fig. 7(b), we show how W and \tilde{A} (defined by Eq. (20)) vary as a function of k and c at $\varepsilon_{st} = 0$. The contour plots indicate that \tilde{A} is large for $k \to 1$ and $c \to c_0$, while W is mostly affected by the velocity c. Furthermore, when investigating the stability of the sn solutions through Eq. (30), we find that only those with relatively small k (and, therefore, small amplitude) are stable (see green area in Fig. 7(a)). To better understand the feature of sn solutions, we focus on waves characterized by four combinations of c and c and plot the evolution of c and c lying within the stable region (i.e. c locations, c locations, c locations, c locations and Eq. (19) (see Fig. 7(c)). For the three combinations of c and c lying within the stable region (i.e. c locations, c locations, c locations, c locations, c locations, c locations are circular markers in Fig. 7(a)) we find that the theoretical predictions perfectly match with numerical results. Furthermore, the numerical results clearly

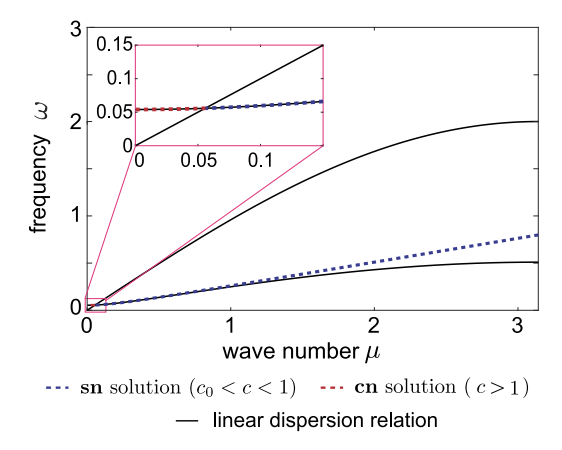


Fig. 8. Dispersion relation derived from cnoidal wave solutions (dashed lines) and from the linearized discrete governing equations (solid lines) for a chain with $\epsilon_{sl} = 0$. (For interpretation of the references to color in this figure legend, the reader is referred to the web version of this article.)

show that waves with k and c outside the stable region are not supported by the system as they largely deviate from the sn solution (see plot for (c, k) = (0.50, 0.60) in Fig. 7(c)).

Next, since all stable sn solutions in the prebuckling regime are characterized $k \to 0$ and $\tilde{A} \to 0$, we study in detail the characteristics of the supported waves in this limit. Again, we start by calculating their frequency in the limit $k \to 0$

$$\lim_{k \to 0} \omega = \lim_{k \to 0} \frac{\pi c}{2K(k)W} = \frac{2\alpha c\sqrt{\varepsilon_{st} + 3K_{\theta}/2}}{\sqrt{c^2 - \alpha^2(K_s - K_{\theta})}},\tag{39}$$

Considering $c = \omega/\mu$, Eq. (39) can be written as

$$\omega^2 - \alpha^2 \mu^2 \left(K_s - K_\theta \right) - 4\alpha^2 \left(\varepsilon_{st} + 3K_\theta / 2 \right) = 0, \tag{40}$$

from which we obtain

$$\omega = \alpha \sqrt{\mu^2 \left(K_s - K_\theta \right) + 4 \left(\varepsilon_{st} + 3K_\theta / 2 \right)},\tag{41}$$

with $\omega/\mu=c\in(c_0,1)$. Importantly, we find that the dispersion relation defined by Eq. (41) overlaps with a portion of that derived directly from the linearized discrete equations of motion (see Fig. 8). Therefore, these results indicate that, as for the dn wave solution, the small amplitude waves to which the sn solution reduces in the prebuckling regime for $k\to 0$ are linear vibrations around $\theta=0$. Note that the rotational and translational components are decoupled for linear waves in the prebuckling regime (see Appendix B). As such the cnoidal wave solutions only recovers the rotational branch, since here we only focus on its rotational component.

5.2. Postbuckling regime

It follows from Eq. (14) that in the postbuckling regime the sn solution exists for $c \in (c_0, 1)$ (see yellow and green areas in Fig. 9(a)). Note that the breakdown of the continuum solution as $c \to c_0$ and $c \to 1$ is due to imaginary width. By substituting Eqs. (13) into Eq. (37) we find that the latter is satisfied only if

$$A = \sqrt{\frac{2k^2}{1+k^2}} \theta_{st} \text{ and } W = \sqrt{\frac{(c^2 - c_0^2)(1-c^2)(1+k^2)}{2\alpha^2 \theta_{st}^2 c^2}}.$$
 (42)

In Fig. 9(b) we report the evolution of \tilde{A} (defined by Eq. (20)) and W as a function of c and k at $\varepsilon=-1.5\times 10^{-3}$ (which corresponds to $\theta_{st}=\pm 0.05$). The plots show that \tilde{A} monotonically increases with k and is marginally affected by c, whereas W is mostly controlled by c. By using Eq. (30) we then find that only the solutions with relatively large k for which $\tilde{A}\to\theta_{st}$ are stable (see green area for stable solutions and yellow for unstable ones in Fig. 9(a)). As shown in Fig. 9(c), for k=1 the cnoidal solutions reduce to topological solitons (kinks) that bring all units from one stable state (characterized by $+\theta_{st}$) to another (characterized by rotations in opposite direction $-\theta_{st}$) (Dauxois and Peyrard, 2006; Deng et al., 2018a) (see results for (c,k)=(0.5,1) and (0.9,1) in Fig. 9(c)). Such topological solitons possess amplitude $\tilde{A}=\theta_{st}$, while their width varies with velocity c (see Figs. 9(b) and (c)). As k is lowered, the sn solution first transforms into waves that periodically oscillate between two stable states (see results for (c,k)=(0.5,0.9) in Fig. 9(c)) and then eventually become unstable (see results for (c,k)=(0.5,0.4) in Fig. 9(c)). Differently, for $c\to c_0$ the solutions with large k are unstable (see results for (c,k)=(0.28,0.31) in Fig. 9(c)). Finally, we note that the lack of stability for solutions with $k\to 1$ and either $c\to c_0$ or $c\to 1$ can be attributed to the small width of such waves (see Fig. 9(b)) for which the continuum assumption made to derive our analytical solution is violated.

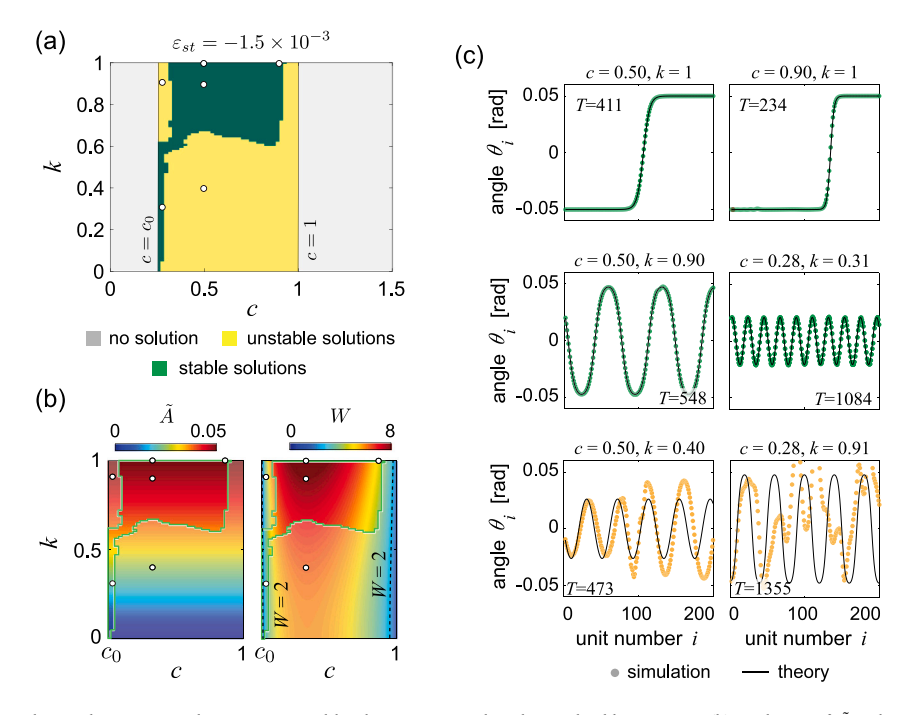


Fig. 9. (a) Effect of c and k on the sn wave solutions supported by the metamaterial in the postbuckling regime. (b) Evolution of \tilde{A} and W as a function of c and k at $\epsilon_{st} = -1.5 \times 10^{-3}$ (with $\theta_{st} = \pm 0.05$). (c) Numerical (markers) and analytical (lines) results for sn solutions propagating in a buckled chain (i.e. $\epsilon_{st} = -1.5 \times 10^{-3}$). Rotation profiles for (c, k) = (0.50, 1), (0.90, 0.71), (0.50, 0.90), (0.28, 0.31), (0.50, 0.40) and (0.28, 0.91). The circular markers in Figs. 9(a) and (b) indicate the points considered in our numerical analysis, whose results are presented in Fig. 9(c). (For interpretation of the references to color in this figure legend, the reader is referred to the web version of this article.)

6. cn solution

Finally, we consider the cn solution defined by Eq. (23). By substituting it into Eq. (5), we find that the latter is satisfied only if

$$2k^2 = -A^2W^2C_3$$
 and $2k^2 - 1 = W^2C_1$. (43)

As such, our system can support the cn wave solutions only if $C_3 < 0$. Further, for $C_1 > 0$ only solutions with $1/\sqrt{2} < k < 1$ are permitted, while for $C_1 < 0$ only solutions with $0 < k < 1/\sqrt{2}$ are allowed.

6.1. Prebuckling regime

It follows from Eqs. (9) and (10) that for this deformation regime the cn wave solutions are supported only if (i) $c \in (0, c_0)$ with $1/\sqrt{2} < k < 1$ and (ii) $c \in (1, \infty)$ with $0 < k < 1/\sqrt{2}$ (see yellow and green areas in Fig. 10(a)) and that for both cases

$$A = \frac{2k}{c} \sqrt{\frac{1 - c^2}{2k^2 - 1} \left(\varepsilon_{st} + \frac{3}{2} K_{\theta}\right)} \text{ and } W = \sqrt{\frac{(c_0^2 - c^2)(2k^2 - 1)}{4\alpha^2 \left(\varepsilon_{st} + \frac{3}{2} K_{\theta}\right)}}.$$
 (44)

In Figs. 10(b) and (c), we show the evolution of \tilde{A} (defined by Eq. (24)) and W at $\varepsilon_{st}=0$ and bound with a green line the solutions that are stable according to Eq. (30) (see also green areas in Fig. 10(a)). We find that for $c \in (0, c_0)$ the cn solutions are only stable for $k \to 1$. For k=1 the cn wave solutions reduces to solitary waves (see results for (c,k)=(0.15,1) in Fig. 10(d)). As k is lowered, trains of solitons emerge (see results for (c,k)=(0.15,0.9999) in Fig. 10(d)), but they quickly become unstable as neighboring peaks have opposite sign. Differently, for $c \in (1,\infty)$ the cn solutions are stable only for $k \to 0$ and are characterized by small \tilde{A} (see Fig. 10(c)). As presented above for the dn and sn solutions, also in this case we verify that these small amplitude cnoidal waves reduce to linear waves. To this end, we evaluate their frequency in the limit $k \to 0$,

$$\lim_{k \to 0} \omega = \lim_{k \to 0} \frac{\pi c}{2K(k)W} = \frac{2\alpha c \sqrt{\varepsilon_{st} + 3K_{\theta}/2}}{\sqrt{c^2 - \alpha^2 (K_s - K_{\theta})}}$$

$$\tag{45}$$

By expressing c as $c = \omega/\mu$, Eq. (39) can be written as

$$\omega^2 - \alpha^2 \mu^2 \left(K_s - K_\theta \right) - 4\alpha^2 \left(\varepsilon_{st} + 3K_\theta / 2 \right) = 0, \tag{46}$$

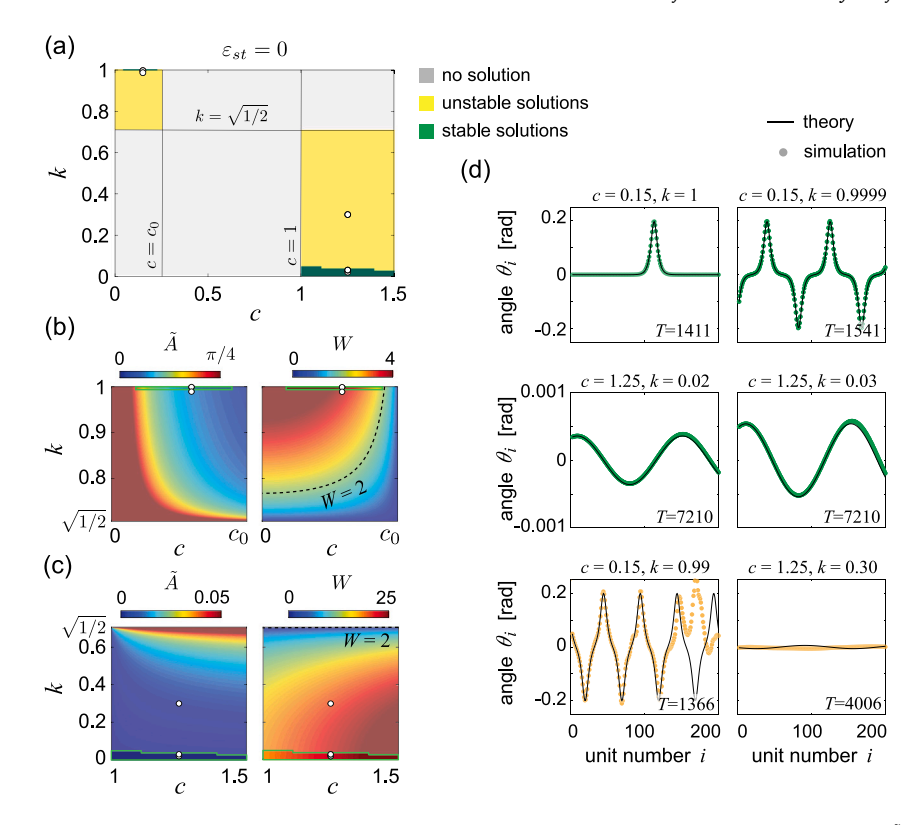


Fig. 10. (a) Effect of c and k on the cn wave solutions supported by the metamaterial in the prebuckling regime. (b)–(c) Evolution of \tilde{A} and W as a function of c and k at $\varepsilon_{st}=0$. (d) Numerical (markers) and analytical (lines) results for cn solutions propagating in an undeformed chain (i.e. $\varepsilon_{st}=0$). Rotation profiles for (c,k)=(0.15,1), (0.15,0.9999), (1.25,0.02), (1.25,0.03), (0.15,0.999) and (1.25,0.30). The circular markers in Figs. 10(a)–(c) indicate the points considered in our numerical analysis, whose results are presented in Fig. 10(d). (For interpretation of the references to color in this figure legend, the reader is referred to the web version of this article.)

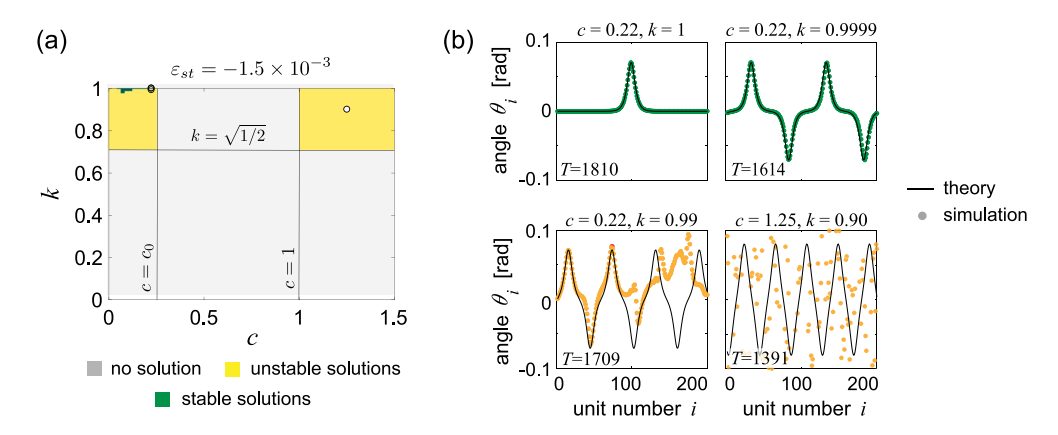


Fig. 11. (a) Effect of c and k on the cn wave solutions supported by the metamaterial in the postbuckling regime. (b) Numerical (markers) and analytical (lines) results for cn solutions propagating in a buckled chain (i.e. $\varepsilon_{st} = -1.5 \times 10^{-3}$). Rotation profiles for (c, k) = (0.22, 1), (0.22, 0.9999), (0.22, 0.9999) and (1.25, 0.99). The circular markers in Fig. 11(a) indicate the points considered in our numerical analysis, whose results are presented in Fig. 11(b). (For interpretation of the references to color in this figure legend, the reader is referred to the web version of this article.)

from which we obtain

$$\omega = \alpha \sqrt{\mu^2 \left(K_s - K_\theta \right) + 4 \left(\varepsilon_{st} + 3K_\theta / 2 \right)},\tag{47}$$

with $\omega/\mu = c \in (1, \infty)$. Note that Eq. (47) is identical to Eq. (41) but since it is valid for a different velocity range it recovers a different portion of the dispersion relations derived directly form the linearized discrete equations (see the red dashed line in Fig. 8)).

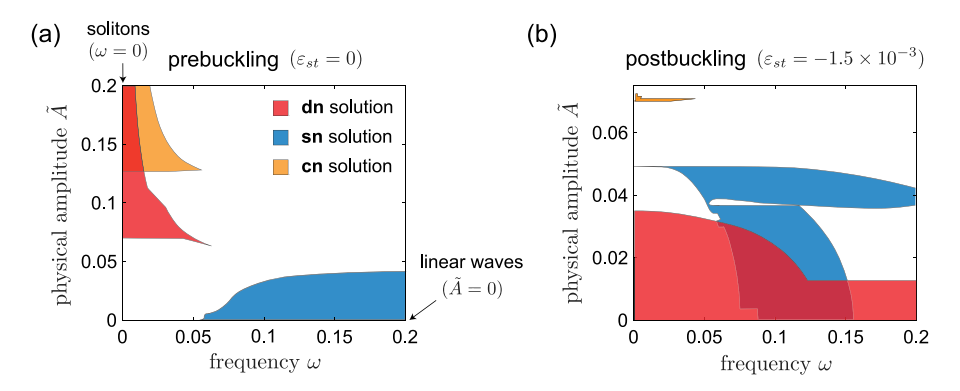


Fig. 12. Stable cnoidal wave solutions in the $\omega \tilde{A}$ space in (a) the prebuckling regime ($\varepsilon_{st} = 0$) and (b) the postbuckling regime ($\varepsilon_{st} = -1.5 \times 10^{-3}$).

6.2. Postbuckling regime

It follows from Eqs. (13) and (14) that for this deformation regime cn wave solutions are supported only if $1/\sqrt{2} < k < 1$ and $c \in (0, c_0) \cup (1, \infty)$ (see yellow and green areas in Fig. 11(a)) and that

$$A = \sqrt{\frac{2k^2}{2k^2 - 1}} \theta_{st} \text{ and } W = \sqrt{\frac{(c_0^2 - c^2)(1 - c^2)(2k^2 - 1)}{2\alpha^2 \theta_{st}^2 c^2}}.$$
 (48)

However, only solutions with $k \to 1$ and $c \in (0, c_0)$ are found to be stable (see green area in Fig. 11(a)) and these correspond to solitary waves and trains of solitons (see Fig. 11(b)).

7. Conclusions

To summarize, we have systematically studied the nonlinear dynamic behavior of flexible mechanical metamaterials. While previous studies have mostly focused either on linear/weakly nonlinear small amplitude vibrations or large amplitude solitary pulses, the proposed framework based on cnoidal waves (which over the last century have found applications in different fields of science and engineering, Whitham, 2011; Clarke, 1971; Wilson et al., 2011; Samsonov, 2001; Remoissenet, 2013; Samsonov, 1994) not only enables us to describe general nonlinear oscillations with both non-vanishing amplitude and nonzero fundamental frequency, but also reduce to phonons and solitons under suitable limits. To further emphasize this point, in Fig. 12 we report all identified stable dn, cn and sn wave solutions in the ω - \tilde{A} space for both the prebuckling (i.e. $\varepsilon_{st}=0$) and postbuckling (i.e. $\varepsilon_{st}=-1.5\times10^{-3}$) regimes. On the horizontal axis of these plots (i.e. $\tilde{A}=0$) we identify the linear waves and recover their frequency band gaps. Differently, on the vertical axis (for which $\omega=0$) we identify the solitary waves and recover their recently observed amplitude gaps (Deng et al., 2018b). Finally, moving away from both axes, we identify the supported periodic nonlinear waves that are found to be stable as well as "amplitude–frequency gap" (i.e. regions in the ω - \tilde{A} space in which nonlinear oscillations fail to stably propagate without distortion — see white regions). Importantly, since the proposed approach is readily applicable to any mechanical system whose response can be described by a nonlinear Klein–Gordon equation, we envision it to be a powerful tool to explore the rich nonlinear dynamic behavior of flexible metamaterials.

Declaration of competing interest

The authors declare that they have no known competing financial interests or personal relationships that could have appeared to influence the work reported in this paper.

Acknowledgments

A part of this research was done when PKP was Visiting Professor at MIT in Fall 2019. PKP thanks the Department of Mechanical Engineering at MIT, USA for their generous support and a seed grant from NSF MRSEC-DMR 1720530. K.B. acknowledges support from NSF, USA grants EFMA-1741685 and DMR-2011754 and Army Research Office, USA Grant W911NF-17-1-0147. J.L. acknowledges support from China Scholarship Council.

Appendix A. Discrete equations of motion

The discrete equations of motion for the chain considered in this study are given by Deng et al. (2018b),

$$\frac{\partial^{2} U_{i}}{\partial T^{2}} = U_{i+1} - 2U_{i} + U_{i-1} - \frac{1}{2} \left(\cos \theta_{i+1} - \cos \theta_{i-1} \right),
\frac{1}{\alpha^{2}} \frac{\partial^{2} \theta_{i}}{\partial T^{2}} = -K_{\theta}(\theta_{i+1} + 4\theta_{i} + \theta_{i-1}) + K_{s} \cos \theta_{i} \left[\sin \theta_{i+1} + \sin \theta_{i-1} - 2 \sin \theta_{i} \right]
- \sin \theta_{i} \left[2 \left(U_{i+1} - U_{i-1} \right) + 4 - \cos \theta_{i+1} - 2 \cos \theta_{i} - \cos \theta_{i-1} \right],$$
(49)

where, to facilitate the analysis, we have defined the positive direction of rotation alternatively for neighboring crosses (i.e., if for the ith top unit a clockwise rotation is positive, then for the (i-1)th and (i+1)th ones counterclockwise rotation is positive). For a structure comprising N pairs of crosses Eqs. (49) results in a system of 2N coupled differential equations, which we numerically solve using the 2nd order Runge–Kutta method (via the Matlab function ode23).

Appendix B. Dispersion relation from the discrete equations of motion

The dispersion relation for our discrete system can be obtained by linearizing Eqs. (49) around the predeformed configurations defined by ε_{st} and θ_{st} (which are related via Eq. (3)). Let us consider a perturbation $\tilde{\theta}_i$ and \tilde{U}_i of the rotation and displacement of the *i*th unit,

$$\tilde{\theta}_i = \theta_i - \theta_{st}$$
, and $\tilde{U}_i = U_i - \varepsilon_{st}i$ (50)

which takes the chain to a new equilibrium configuration where Eqs. (49) are still satisfied. For such small perturbations

$$\frac{\sin(\tilde{\theta}_{i+p} + \theta_{st}) \approx \sin \theta_{st} + \cos \theta_{st} \ \tilde{\theta}_{i+p}}{\cos(\tilde{\theta}_{i+p} + \theta_{st}) \approx \cos \theta_{st} - \sin \theta_{st} \ \tilde{\theta}_{i+p}},$$
(51)

where $p \in \{-1, 0, 1\}$. Substitution of Eq. (50) and (51) into Eqs. (49) yields

$$\frac{\partial^{2} \tilde{U}_{i}}{\partial T^{2}} = \tilde{U}_{i+1} - 2\tilde{U}_{i} + \tilde{U}_{i-1} + \frac{1}{2} \sin \theta_{st} \left(\tilde{\theta}_{i+1} - \tilde{\theta}_{i-1} \right),$$

$$\frac{1}{\alpha^{2}} \frac{\partial^{2} \tilde{\theta}_{i}}{\partial T^{2}} = \left(K_{s} \cos^{2} \theta_{st} - \sin^{2} \theta_{st} - K_{\theta} \right) \left(\tilde{\theta}_{i+1} + \tilde{\theta}_{i-1} \right) - 2 \sin \theta_{st} \left(\tilde{U}_{i+1} - \tilde{U}_{i-1} \right)$$

$$- 4 \left(\frac{K_{s} \cos^{2} \theta_{st}}{2} + \frac{\sin^{2} \theta_{st}}{2} + K_{\theta} + \varepsilon_{st} + 1 - \cos \theta_{st} \right) \tilde{\theta}_{i}$$
(52)

which are the linearized equations of motion for around the predeformed configurations defined by ϵ_{st} and θ_{st} . Eqs. (52) can be written in matrix form as

$$\mathbf{M}\ddot{\boldsymbol{\Phi}}_{i} + \sum_{p=-1,0,1} \mathbf{K}^{(p)} \boldsymbol{\Phi}_{i+p} = 0,$$
 (53)

where

$$\mathbf{M} = \begin{bmatrix} 1 & 0 \\ 0 & \alpha^{-2} \end{bmatrix}, \quad \boldsymbol{\Phi}_{i+p} = \begin{bmatrix} \tilde{U}_{i+p} \\ \tilde{\theta}_{i+p} \end{bmatrix}, \quad \mathbf{K}^{(0)} = \begin{bmatrix} 2 & 0 \\ 0 & R \end{bmatrix} \quad \text{and} \quad \mathbf{K}^{(\pm 1)} = \begin{bmatrix} -1 & \mp \frac{1}{2} \sin \theta_{st} \\ \pm 2 \sin \theta_{st} & -Q \end{bmatrix}. \tag{54}$$

with

$$R = 4\left(\frac{K_s \cos^2 \theta_{st}}{2} + \frac{\sin^2 \theta_{st}}{2} + K_\theta + \varepsilon_{st} + 1 - \cos \theta_{st}\right),$$

$$Q = K_s \cos^2 \theta_{st} - \sin^2 \theta_{st} - K_\theta.$$
(55)

Next, we seek a solution of Eqs. (53) in the form of a harmonic wave

$$\boldsymbol{\Phi}_{i}(T) = \hat{\boldsymbol{\Phi}}_{i}(\mu) \exp \iota(\mu i - \omega T), \tag{56}$$

where ω is the normalized cyclic frequency of harmonic motion (the dimensional cyclic frequency is $\omega \sqrt{k_l/m}$), μ is the wavenumber, $\iota = \sqrt{-1}$ and $\hat{\Phi}_i$ is a vector that defines the amplitude of wave motion. Substitution of Eq. (56) into Eq. (53) yields

$$-\omega^2 \mathbf{M} \hat{\boldsymbol{\phi}}_i + \sum_{p=-1,0,1} \mathbf{K}^{(p)} \hat{\boldsymbol{\phi}}_{i+p} e^{i\mu(i+p)} = 0.$$
 (57)

Eq. (57) defines an eigenvalue problem that yields two dispersion branches, $\omega^{(1)}(\mu)$ and $\omega^{(2)}(\mu)$, each corresponding to a linear wave mode.

For the prebuckling regime (for which $\theta_{st} = 0$) Eq. (57) admits analytical solution

$$\omega^{(1)} = \sqrt{2 - 2\cos\mu} \text{ or } \omega^{(2)} = \alpha \sqrt{4\left(\frac{K_s}{2} + K_{\theta} + \epsilon_{st}\right) - 2(K_s - K_{\theta})\cos\mu}.$$
 (58)

Differently, for the postbuckling (for which $\theta_{st} \neq 0$) Eq. (57) can only be solved numerically to obtain $\omega^{(1)}$ and $\omega^{(2)}$.

Appendix C. Other types of cnoidal wave solutions

To demonstrate that cn, sn and dn are the only three independent cnoidal wave solutions of Eq. (5), here we show that other cnoidal wave solutions such as 1/dn, cn/dn and sn/dn, reduce to those except for a phase shift.

1/dn solution: To begin with, with we consider a solution with form

$$\theta(\zeta) = \frac{A_{1/\text{dn}}}{\text{dn}\left(\frac{\zeta}{W_{1/\text{dn}}} \mid k\right)}.$$
(59)

By substituting of Eq. (59) into Eq. (5), we find that the latter is identically satisfied only if

$$1 - k^2 = -\frac{A_{1/dn}^2 W_{1/dn}^2}{2} C_3, \text{ and } 2 - k^2 = W_{1/dn}^2 C_1.$$
 (60)

By comparing Eqs. (60) to the corresponding constraints derived for the dn solution (Eq. (27)), we obtain

$$A_{1/\text{dn}} = \sqrt{1 - k^2} A$$

$$W_{1/\text{dn}} = W$$
(61)

Furthermore, since (Abramowitz et al., 1988)

$$\frac{1}{\text{dn}(x|k)} = \frac{\text{dn}(x - 2K(k)|k)}{\sqrt{1 - k^2}}, \ \forall x$$
 (62)

it follows that the solution given in Eq. (59) can be rewritten as

$$\frac{A_{1/\text{dn}}}{\text{dn}\left(\frac{\zeta}{W_{1/\text{dn}}}|k\right)} = A_{\text{dn}} \, \text{dn}\left(\frac{\zeta}{W_{\text{dn}} - 2K(k)}|k\right). \tag{63}$$

Eq. (63) clearly show that the 1/dn solution given in Eq. (59) is identical to the dn solution presented in Eq. (15) except for a phase shift

cn/dn solution: Next, we consider a solution with form

$$\theta(\zeta) = A_{\text{cn/dn}} \frac{\text{cn}\left(\frac{\zeta}{W_{\text{cn/dn}}} \middle| k\right)}{\text{dn}\left(\frac{\zeta}{W_{\text{cn/dn}}} \middle| k\right)}.$$
(64)

By substituting of Eq. (64) into Eq. (5), we find that the latter is identically satisfied only if

$$2k^2 = A_{\rm cn/dn}^2 W_{\rm cn/dn}^2 C_3$$
, and $1 + k^2 = -W_{\rm cn/dn}^2 C_1$. (65)

By comparing Eqs. (65) to the corresponding constraints derived for the sn solution (Eq. (37)), we obtain

$$A_{\text{cn/dn}} = A$$
 and $W_{\text{cn/dn}} = W$. (66)

Furthermore, since (Abramowitz et al., 1988)

$$\frac{\operatorname{cn}(x|k)}{\operatorname{dn}(x|k)} = \operatorname{sn}(x + K(k)|k), \quad \forall x,$$
(67)

it follows that the solution given in Eq. (64) can be rewritten as

$$A_{\text{cn/dn}} \frac{\operatorname{cn}\left(\frac{\zeta}{W_{\text{cn/dn}}} \mid k\right)}{\operatorname{dn}\left(\frac{\zeta}{W_{\text{cn/dn}}} \mid k\right)} = A \operatorname{sn}\left(\frac{\zeta}{W} + K(k) \mid k\right). \tag{68}$$

Eq. (68) clearly show that the cn/dn solution given in Eq. (64) is identical to the sn solution presented in Eq. (19) except for a phase shift

sn/dn solution: Finally, we consider a solution with form

$$\theta(\zeta) = A_{\text{sn/dn}} \frac{\text{sn}\left(\frac{\zeta}{W_{\text{sn/dn}}} \middle| k\right)}{\text{dn}\left(\frac{\zeta}{W_{\text{sn/dn}}} \middle| k\right)},\tag{69}$$

By substituting of Eq. (69) into Eq. (5), we find that the latter is identically satisfied only if

$$2k^{2}(k^{2}-1) = A_{\rm sn/dn}^{2}W_{\rm sn/dn}^{2}C_{3}, \text{ and } 2k^{2}-1 = W_{\rm sn/dn}^{2}C_{1}.$$

$$(70)$$

By comparing Eqs. (70) to the corresponding constraints derived for the cn solution (Eq. (43)), we obtain

$$A_{\rm sn/dn} = \sqrt{1 - k^2} A$$
 and $W_{\rm sn/dn} = W$. (71)

Furthermore, since (Abramowitz et al., 1988)

$$\frac{\operatorname{sn}(x|k)}{\operatorname{dn}(x|k)} = \frac{\operatorname{cn}\left(x - K(k)|k\right)}{\sqrt{1 - k^2}}, \ \forall x$$
 (72)

it follows that the solution given in Eq. (69) can be rewritten as

$$A_{\text{sn/dn}} \frac{\operatorname{sn}\left(\frac{\zeta}{W_{\text{sn/dn}}} \middle| k\right)}{\operatorname{dn}\left(\frac{\zeta}{W_{\text{sn/dn}}} \middle| k\right)} = A \operatorname{cn}\left(\frac{\zeta}{W} \middle| k\right)$$
(73)

Eq. (73) clearly show that the cn/dn solution given in Eq. (64) is identical to the cn solution presented in Eq. (23) except for a phase shift.

Appendix D. Supplementary data

Supplementary material related to this article can be found online at https://doi.org/10.1016/j.jmps.2020.104233.

References

Abramowitz, M., Stegun, I.A., Romer, R.H., 1988. Handbook of Mathematical Functions with Formulas, Graphs, and Mathematical Tables. American Association of Physics Teachers.

Allein, F., Tournat, V., Gusev, V., Theocharis, G., 2020. Linear and nonlinear elastic waves in magnetogranular chains. Phys. Rev. A 13 (2), 024023.

Bertoldi, K., Boyce, M., 2008. Mechanically triggered transformations of phononic band gaps in periodic elastomeric structures. Phys. Rev. B 77 (5), 052105.

Bertoldi, K., Vitelli, V., Christensen, J., van Hecke, M., 2017. Flexible mechanical metamaterials. Nature Rev. Mater. 2 (11), 17066. Bückmann, T., Kadic, M., Schittny, R., Wegener, M., 2015. Mechanical cloak design by direct lattice transformation. Proc. Natl. Acad. Sci. 112 (16), 4930–4934.

Cabaret, J., Béquin, P., Theocharis, G., Andreev, V., Gusev, V., Tournat, V., 2015. Nonlinear hysteretic torsional waves. Phys. Rev. Lett. 115 (5), 054301.

Cabaret, J., Tournat, V., Béquin, P., 2012. Amplitude-dependent phononic processes in a diatomic granular chain in the weakly nonlinear regime. Phys. Rev. E 86 (4), 041305.

Celli, P., Gonella, S., 2015. Manipulating waves with LEGO® bricks: A versatile experimental platform for metamaterial architectures. Appl. Phys. Lett. 107 (8),

Chen, Z., Guo, B., Yang, Y., Cheng, C., 2014a. Metamaterials-based enhanced energy harvesting: A review. Physica B 438, 1-8.

Chen, B.G.-g., Upadhyaya, N., Vitelli, V., 2014b. Nonlinear conduction via solitons in a topological mechanical insulator. Proc. Natl. Acad. Sci. 111 (36), 13004–13009

Christensen, J., Kadic, M., Kraft, O., Wegener, M., 2015. Vibrant times for mechanical metamaterials. MRS Commun. 5 (3), 453-462.

Clarke, R., 1971. Solitary and cnoidal planetary waves. Geophys. Fluid Dyn. 2 (1), 343-354.

Clausen, A., Wang, F., Jensen, J.S., Sigmund, O., Lewis, J.A., 2015. Topology optimized architectures with programmable Poisson's ratio over large deformations. Adv. Mater. 27 (37), 5523–5527.

Coulais, C., Kettenis, C., van Hecke, M., 2018. A characteristic length scale causes anomalous size effects and boundary programmability in mechanical metamaterials. Nat. Phys. 14 (1), 40–44.

Dauxois, T., Peyrard, M., 2006. Physics of Solitons. Cambridge University Press.

Deng, B., Mo, C., Tournat, V., Bertoldi, K., Raney, J.R., 2019. Focusing and mode separation of elastic vector solitons in a 2D soft mechanical metamaterial. Phys. Rev. Lett. 123 (2), 024101.

Deng, B., Raney, J., Tournat, V., Bertoldi, K., 2017. Elastic vector solitons in soft architected materials. Phys. Rev. Lett. 118 (20), http://dx.doi.org/10.1103/PhysRevLett.118.204102.

Deng, B., Tournat, V., Bertoldi, K., 2018a. Effect of predeformation on the propagation of vector solitons in flexible mechanical metamaterials. Phys. Rev. E 98 (5), 053001.

Deng, B., Tournat, V., Wang, P., Bertoldi, K., 2019b. Anomalous collisions of elastic vector solitons in mechanical metamaterials. Phys. Rev. Lett. 122 (4), 044101. Deng, B., Wang, P., He, Q., Tournat, V., Bertoldi, K., 2018b. Metamaterials with amplitude gaps for elastic solitons. Nature Commun. 9, 3410. http://dx.doi.org/10.1038/s41467-018-05908-9.

Deng, B., Zhang, Y., He, Q., Tournat, V., Wang, P., Bertoldi, K., 2019c. Propagation of elastic solitons in chains of pre-deformed beams. New J. Phys..

D'Errico, J., 2013. Distance2curv (v 1.1.0): Find the closest point on a (n-dimensional) curve to any given point or set of points. MATLAB Central File Exchange. https://www.mathworks.com/matlabcentral/fileexchange/34869-distance2curve.

Grima, J.N., Evans, K.E., 2000. Auxetic Behavior from Rotating Squares.

Lakes, R.S., Lee, T., Bersie, A., Wang, Y.-C., 2001. Extreme damping in composite materials with negative-stiffness inclusions. Nature 410 (6828), 565-567.

Melo, F., Job, S., Santibanez, F., Tapia, F., 2006. Experimental evidence of shock mitigation in a Hertzian tapered chain. Phys. Rev. E 73 (4), 041305.

Mo, C., Singh, J., Raney, J.R., Purohit, P.K., 2019a. Cnoidal wave propagation in an elastic metamaterial. Phys. Rev. E 100 (1), 013001.

Narisetti, R.K., Leamy, M.J., Ruzzene, M., 2010. A perturbation approach for predicting wave propagation in one-dimensional nonlinear periodic structures. J. Vib. Acoust. 132 (3).

Parkes, E., 1991. The modulational instability of the nonlinear Klein-Gordon equation. Wave Motion 13 (3), 261-275.

Remoissenet, M., 2013. Waves Called Solitons: Concepts and Experiments. Springer Science & Business Media.

Samsonov, A., 1994. Nonlinear strain waves in elastic waveguides. In: Nonlinear Waves in Solids. Springer, pp. 349–382.

Samsonov, A.M., 2001. Strain Solitons in Solids and how to Construct Them. CRC Press.

Sánchez-Morcillo, V.J., Pérez-Arjona, I., Romero-García, V., Tournat, V., Gusev, V., 2013. Second-harmonic generation for dispersive elastic waves in a discrete granular chain. Phys. Rev. E 88 (4), 043203.

Sun, H., Du, X., Pai, P.F., 2010. Theory of metamaterial beams for broadband vibration absorption. J. Intell. Mater. Syst. Struct. 21 (11), 1085-1101.

Theocharis, G., Boechler, N., Daraio, C., 2013. Nonlinear periodic phononic structures and granular crystals. In: Acoustic Metamaterials and Phononic Crystals. Springer, pp. 217–251.

Wang, P., Casadei, F., Shan, S., Weaver, J.C., Bertoldi, K., 2014. Harnessing buckling to design tunable locally resonant acoustic metamaterials. Phys. Rev. Lett. 113 (1), 014301.

Wang, Z., Zhang, Q., Zhang, K., Hu, G., 2016. Tunable digital metamaterial for broadband vibration isolation at low frequency. Adv. Mater. 28 (44), 9857–9861. Whitham, G.B., 2011. Linear and Nonlinear Waves, Vol. 42. John Wiley & Sons.

- Wilson, M., Aboites, V., Pisarchik, A.N., Ruiz-Oliveras, F., Taki, M., 2011. Stable cnoidal wave formation in an erbium-doped fiber laser. Appl. Phys. Express 4 (11), 112701.
- Yasuda, H., Miyazawa, Y., Charalampidis, E.G., Chong, C., Kevrekidis, P.G., Yang, J., 2019. Origami-based impact mitigation via rarefaction solitary wave creation. Sci. Adv. 5 (5), eaau2835.
- Zhang, Y., Li, B., Zheng, Q., Genin, G.M., Chen, C., 2019. Programmable and robust static topological solitons in mechanical metamaterials. Nature Commun. 10 (1), 1–8.